J Mater Sci (2007) 42:1415–1426
DOI 10.1007/s10853-006-1118-0

Deformation behavior and mechanisms of a nanocrystalline multi-phase aluminum alloy

Leon L. Shaw · Hong Luo

Received: 2 June 2006 / Accepted: 10 October 2006 / Published online: 3 January 2007

Abstract A nanocrystalline (nc) Al–Fe–Cr–Ti alloy containing 30 vol.% nc intermetallic particles has been used to investigate deformation behavior and mechanisms of nc multi-phase alloys. High compressive strengths at room and elevated temperatures have been demonstrated. However, tensile fracture strengths below 300 °C are lower than the corresponding maximum strengths in compression. Creep flow of the nc fcc-Al grains is suppressed even though rapid dynamic recovery has occurred. It is argued that the compressive strength at ambient temperature is controlled by propagation of dislocations into nc fcc-Al grains, whereas the compressive strength at elevated temperature is determined by dislocation propagation as well as dynamic recovery. The low tensile fracture strengths and lack of ductility at temperatures below 300 °C are attributed to the limited dislocation storage capacity of nanoscale grains. Since the deformation of the nc Al-alloy is controlled by dislocation propagation into nc fcc-Al grains, the smaller the grain size, the higher the strength. This new microstructural design methodology coupled with ductility-improving approaches could present opportunities for exploiting nc materials in structural applications at both ambient and elevated temperatures.

L. L. Shaw (✉) · H. Luo
Department of Materials Science and Engineering,
University of Connecticut, Storrs, CT 06269, USA
e-mail: Leon.Shaw@UConn.Edu

Introduction

Deformation mechanisms of nanocrystalline (nc) metals and alloys (with grain size <100 nm) have been the subject of intensive study in recent years because of the superior mechanical properties of nc metals and alloys [1–5]. Both experimental studies and theoretical modeling and simulations have been applied to uncover deformation mechanisms of nc metals and alloys [6–20]. These studies have revealed that many unusual deformation mechanisms that are not operative in microcrystalline (mc) metals and alloys (with grain size >1 μm) become operative in nc counterparts. Prominent examples of this kind are deformation twinning and wide stacking faults observed in nc pure aluminum [15–17]. The propensity for localized deformation in the form of shear banding in ultrafine crystalline (ufc) Fe and Ti (with grain size in the 100–1,000 nm range) as well as in nc Fe and Ti is another example of deformation mechanisms in nc and ufc materials which are different from those in mc counterparts [18–20]. All of these studies, however, focus on nc single-phase metals and alloys. In contrast, investigation on deformation mechanisms of nc multi-phase alloys is scarce.

In spite of limited research on deformation mechanisms of nc multi-phase alloys, such nc alloys are expected to find widespread applications because of their stable microstructures derived from second phase drag. Nano-aluminum grains (20–100 nm) in the $Al_{93}Fe_3Ti_2Cr_2$ alloy containing 30 vol.% Al_6Fe and Al_3Ti nano-particles are indeed found to remain at the nanoscale after exposure to a temperature as high as $0.77T_m$ (where T_m is the absolute melting temperature) [21]. Similarly, nanograins of the commercially pure Al (50–60 nm) produced by mechanical alloying can also

be stabilized up to $0.78T_m$ due to the presence of second phase particles formed during mechanical alloying [22]. Ultrafine-grained intermetallics (e.g., γ-TiAl with the average grain size of 196 nm) are also found to be stabilized by $Ti_5(Si,Al)_3$ precipitates along grain boundaries so that superplastic forming can be performed at relatively low temperatures [23]. To benefit from the stable microstructures of multi-phase alloys for engineering applications and materials processing, there is a critical need for developing a fundamental understanding of deformation behavior and mechanisms of nc multi-phase alloys.

With the need above in mind, a nc $Al_{93}Fe_3Ti_2Cr_2$ alloy has been selected as a model system and investigated systematically by several groups including ours [21, 24–31]. In this paper the previous works on the thermal stability [21], tension/compression behaviors [28, 29], and elastic modulus [30] of this multi-phase alloy are reviewed first. The detailed TEM analysis is then presented to elucidate deformation mechanisms of this nc multi-phase alloy as a function of temperature up to $0.7T_m$. Based on the TEM analysis and mechanical testing, a new dislocation-mediated model is then proposed to account for the high compressive strengths observed at both room and elevated temperatures. The model is subsequently extended to providing explanations for the observed difference in the tension and compression behavior. Finally, the future research focus of this nc multi-phase aluminum alloy is discussed.

Experimental procedure

The nc $Al_{93}Fe_3Ti_2Cr_2$ alloy was prepared by mechanical alloying of a mixture of crystalline elemental Al, Fe, Cr and Ti powders in a Szegvari attritor. Both the canister of the attritor and balls 4.76 mm in diameter were made of the stainless steel. A ball-to-powder weight ratio of 20:1 and a milling speed of 600 RPM with the milling duration of 30 h were employed in the experiment. During milling the canister was cooled using circulation water with a flow rate of about 770 mL/min throughout the process and an argon atmosphere was employed. To prevent excessive cold welding, 1.2 wt% stearic acid [$CH_3(CH_2)_{16}COOH$] was added to the powder mixture as the process control agent [31].

Hot extrusion was used to convert the MA-processed powder to bulk material. Prior to extrusion, the MA-processed powder was packed within a metal can and subjected to degassing which was carried out at a temperature ranging from 400 °C to 550 °C until the pressure of the can was reduced to 10^{-5} torr. The parameters controlled during extrusion included the included angle of the extrusion dies, extrusion temperature, extrusion ratio and strain rate. More details of the optimization of the extrusion process can be found in Ref. 28. Two extrusion temperatures, 450 °C and 500 °C, were used to obtain nc-$Al_{93}Fe_3Ti_2Cr_2$ alloys with two different average grain sizes. These extruded $Al_{93}Fe_3Ti_2Cr_2$ bars with two different average grain sizes were used to investigate the effect of the grain size on mechanical properties.

The mechanical properties of the nc $Al_{93}Fe_3Ti_2Cr_2$ alloy were evaluated via compression and tension tests. Cylindrical compressive specimens had dimensions of 6 mm in diameter and 9 mm in height, whereas flat tensile specimens had gauge dimensions of 50 mm in length and 3 mm in thickness. Both ends of the compressive specimens were polished to mirror surfaces and coated with MoS_2 before tests to reduce the interfacial friction. The compressive test was terminated if the specimen did not fracture at –0.45 true strain. All the tests were displacement controlled with a constant strain rate achieved by continuous adjustment in the displacement rate according to the instant height or length of the specimen. The test temperature and strain rate investigated ranged from 25 °C to 400 °C and from 10^{-4} s^{-1} to 10^{-2} s^{-1}, respectively.

The microstructure of the $Al_{93}Fe_3Ti_2Cr_2$ alloy before and after extrusion was examined using a field-emission SEM (Jeol 6335 FESEM). Analyses of the grain size, crystal structure and chemical composition within the microstructure of the Al alloy were also performed using a TEM (JEOL 2010 FASTEM) operating at 200 kV. In the TEM analysis, both bright and dark field image techniques coupled with selected area diffraction (SAD), convergent beam electron diffraction (CBED) and EDS with an electron beam of about 3 nm were utilized. To enhance the image contrast, most of the high-resolution TEM images were reconstructed from Fast Fourier Transformation, during which the diffuse scattering from the background or inelastic scattering was filtered. TEM thin film samples were prepared via standard mechanical polishing down to 100 μm thick discs, followed by jet electro-polishing to electron transparency at –30 °C using an electrolyte of 4% perchloric acid and 96% methanol.

The Young's modulus of the nc $Al_{93}Fe_3Ti_2Cr_2$ alloy as a function of temperature was measured on dynamic mechanical analyzer (DMA) 2980 from TA Instruments in argon environment and at a speed of 3 °C per minute. Furthermore, both the density and chemical composition of the extruded $Al_{93}Fe_3Cr_2Ti_2$ alloy were measured to ensure that the extruded alloy reached full density and contained a minimum of oxygen and

carbon. The density was measured on the basis of Archimedes's principle, whereas the chemical analysis was performed using inductively coupled plasma-optical emission spectroscopy (ICP) in triplicate.

Results and discussion

Microstructure and thermal stability of the NC aluminum alloy

Figure 1 shows bright-field TEM images of the MA-processed $Al_{93}Fe_3Ti_2Cr_2$ alloy before and after extrusion at 500 °C. The selected area diffraction (SAD) patterns and energy dispersive spectrometry (EDS) analysis are also included in Fig. 1. As seen from Fig. 1, the $Al_{93}Fe_3Ti_2Cr_2$ alloy before the extrusion is composed of single phase fcc-Al with grain sizes ranging from 6 nm to 45 nm [21, 26]. The EDS analysis reveals that the nano-grained fcc-Al is the Al-based solid solution containing Fe, Cr and Ti alloying elements. After extrusion, the concentrations of Fe, Ti and Cr in fcc-Al grains have reduced to a level not discernable by the EDS analysis, while precipitation of Al_3Ti and $Al_{13}Fe_4$ intermetallics with Cr solutes has been identified [21]. The $Al_{13}Fe_4$ precipitates have a slightly elongated morphology (Fig. 1e), whereas the Al_3Ti precipitates are equiaxed with particle sizes ranging from 15 nm to 80 nm, slightly smaller than the sizes of $Al_{13}Fe_4$ particles (Fig. 1e and f). The volume fractions of Al_3Ti and $Al_{13}Fe_4$ precipitates have been estimated to be 12% and 18%, respectively, which is consistent with the fact of the extremely low equilibrium solubility of Fe, Cr and Ti in fcc-Al (0.03 at.% Fe,

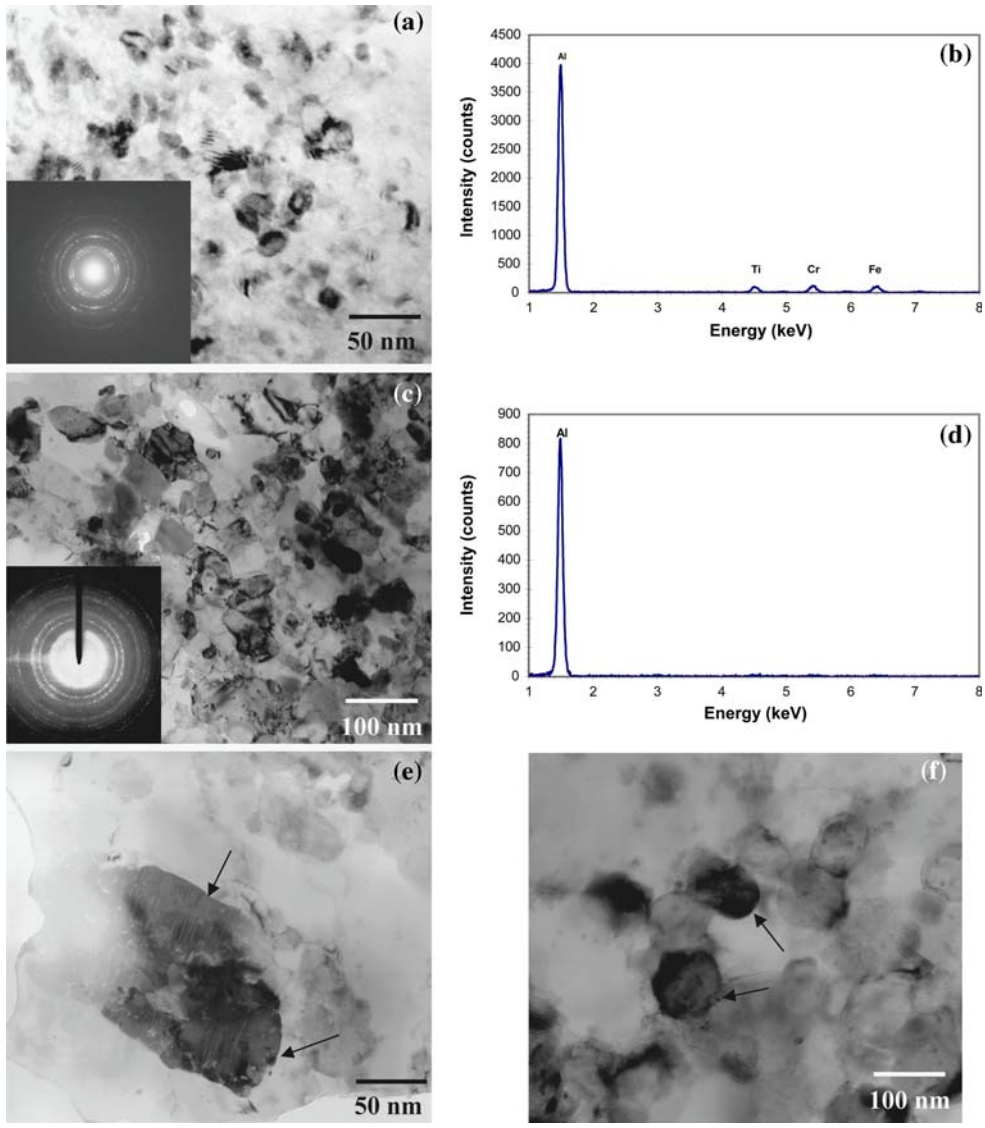

Fig. 1 (**a**) Bright-field TEM image and (**b**) EDS spectrum of the MA-processed $Al_{93}Fe_3Cr_2Ti_2$ alloy before extrusion. The inset SAD pattern in (**a**) corresponds to fcc-Al. (**c**) Bright-field TEM image of the extruded nc $Al_{93}Fe_3Cr_2Ti_2$ alloy, the insert SAD pattern indicating the presence of fcc-Al, $Al_{13}Fe_4$ and Al_3Ti. (**d**) EDS spectrum from a fcc-Al grain in the extruded nc $Al_{93}Fe_3Cr_2Ti_2$ alloy. (**e**) and (**f**) are bright-field TEM images of $Al_{13}Fe_4$ and Al_3Ti precipitates (marked with arrows) in the extruded nc $Al_{93}Fe_3Cr_2Ti_2$ alloy, respectively

>0.01 at.% Cr, and >0.2 at.% Ti) [32] and the assumption of the presence of all Fe and Ti in the intermetallic precipitates.

In addition to the phase transformation during hot extrusion, the fcc-Al grains have grown to 20–150 nm, as shown in Fig. 1c. However, it is noted that in spite of severe plastic deformation and grain growth during the extrusion process, the final fcc-Al grains possess few dislocations (Figs. 1c and 2). This is a strong evidence of dynamic recovery during hot extrusion and will be discussed more in Sect. ''TEM analysis of the deformed NC multi-phase Al-alloy.''

Ball milling and subsequent powder handling during hot extrusion also introduce carbon (0.949 wt.%), oxygen (0.840 wt.%) and nitrogen (0.0175 wt.%) to the Al-alloy powder [28]. These carbon and oxygen impurities could result in the formation of 3.73 vol.% (3.79 wt%) Al_4C_3 and 1.42 vol.% (1.78 wt.%) Al_2O_3 in the extruded Al bars if it is assumed that all the carbon and oxygen in the milled powder react with Al to form these compounds during hot extrusion [28]. The microstructure of the nc multi-phase Al-alloy is very stable because of the oxide, carbide and intermetallic precipitates which have pinned grain boundaries and prevented grain growth during extrusion. In fact, even after exposure to a temperature as high as 600 °C ($0.93T_m$), some of nc-Al grains remain below 50 nm, as revealed from the TEM analysis [21].

Based on Archimedes's principle, the density of the extruded alloy was measured to be 2.92 g/cm^3. This density value is almost identical to 2.91 g/cm^3 calculated from the rule of mixtures with the assumptions that all Fe and Ti are present in the intermetallics. This result indicates the attainment of the full density of the extruded alloy and is in good agreement with the SEM observation, which shows no porosity in the alloy before etching [28].

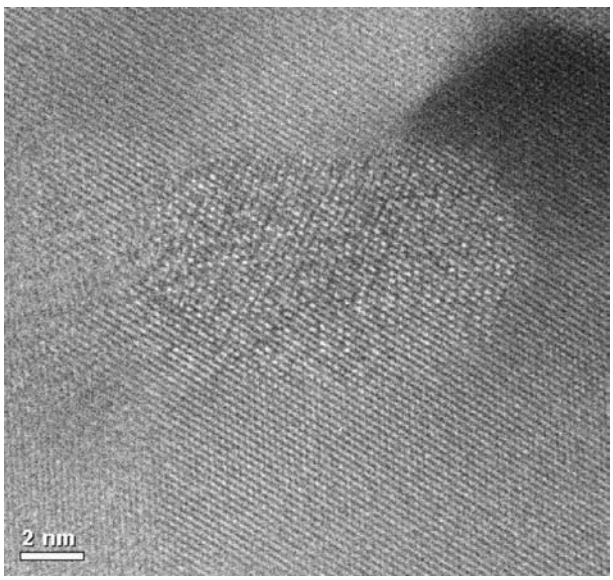

Fig. 2 High resolution TEM image of the extruded nc $Al_{93}Fe_3Cr_2Ti_2$ alloy, showing nc fcc-Al grains free of dislocations

Tensile and compressive behaviors of the NC multi-phase Al-alloy

Figure 3 shows the typical compressive true stress-true strain curves of the extruded nc $Al_{93}Fe_3Ti_2Cr_2$ alloy deformed at different temperatures with a constant strain rate of 10^{-3} s^{-1} [28, 29]. The strength data including the proportionality limit, 0.2% offset yield strength and maximum strength measured from the samples extruded at 500°C are summarized in Table 1. Included in Table 1 are also the strain to the maximum strength and the strain hardening coefficient determined near the onset of 0.2% offset yielding. Several features are noted from these stress-strain curves and Table 1. First, the nc $Al_{93}Fe_3Ti_2Cr_2$ alloy exhibits large compressive strains in all the tests. No cracks form at the surface even after a true strain of –0.45 at which the test is terminated. Examination of the interior of the specimens also results in no evidence of micro- and macro-cracks although some strain softening is present in the compressive stress-strain curves [29]. Second, the maximum strength is high at all temperatures. The maximum strengths at temperatures above 200 °C are especially impressive, because all the current commercial Al alloys lose their useful strengths at temperatures above 200 °C (typically < 100 MPa at 300 °C) [33]. The maximum strengths at elevated temperatures are also higher than that exhibited by Al–Ti–Cu [34], Al–Fe–Ce [35], Al–Fe–V–Si [36] and dispersion-strengthened Al alloys [37]. Third, there is a high work hardening rate after yielding, i.e., the strain hardening coefficient (n = 0.31 at room temperature) is substantially higher than that exhibited by the commercial mc Al alloys (n = 0.15–0.25 at room temperature) [38]. Fourth, the work hardening rate decreases with increasing temperature. Fifth, the strength increases with increasing strain rate. Sixth, the true strain to the maximum strength is small in all cases (about 0.03 or less).

A comparison between Figs. 3a and b also reveals that the strength of the extruded $Al_{93}Fe_3Cr_2Ti_2$ alloys is grain size dependent. The maximum strength for the $Al_{93}Fe_3Cr_2Ti_2$ alloy with an average grain size of 80 nm (Fig. 3a) is about 670 MPa at room temperature, while the corresponding value for the $Al_{93}Fe_3Cr_2Ti_2$ alloy with an average grain size of 50 nm (Fig. 3b) is about

Table 1 The measured mechanical properties from compression tests of the nc Al-alloy with an average grain size of 80 nm at different temperatures with a strain rate of 10^{-3} s^{-1} and the predicted flow stresses from various models

Temperature (°C)	25	200	300	400
Proportionality limit, σ_{PL} (MPa)	440	305	200	125
0.2% Offset yield strength, $\sigma_{0.002}$ (MPa)	562	404	260	168
Maximum strength, σ_{max} (MPa)	665	460	310	186
Strain to the maximum strength, ε @ σ_{max}	0.028	0.030	0.025	0.018
Strain hardening coefficient near the yield point, n	0.31	0.30	0.28	0.25
Predicted flow stress from Coble creep (MPa)	21,768	0.123	0.003	3.1E-4
Predicted flow stress from Nabarro–Herring creep (MPa)	6.3E12	6,206	13.8	0.19
Predicted flow stress from power-law creep (MPa)	21,640	179	42.8	15.4
Predicted τ_{max} for the dislocation propagation (MPa)	291	264	248	232
Predicted stress, σ_c, for departure from the linearity of the stress-strain curve (MPa)	434	351	281	233

690 MPa. Therefore, this set of data indicates that the smaller the grain size, the higher the strength. The same conclusion holds for all the other temperatures tested. For example, the maximum strengths for the $Al_{93}Fe_3Cr_2Ti_2$ alloy with an average grain size of 80 nm are 445 MPa and 320 MPa at 200 °C and 300 °C, respectively, whereas the corresponding values for the $Al_{93}Fe_3Cr_2Ti_2$ alloy with an average grain size of 50 nm are 520 MPa and 340 MPa.

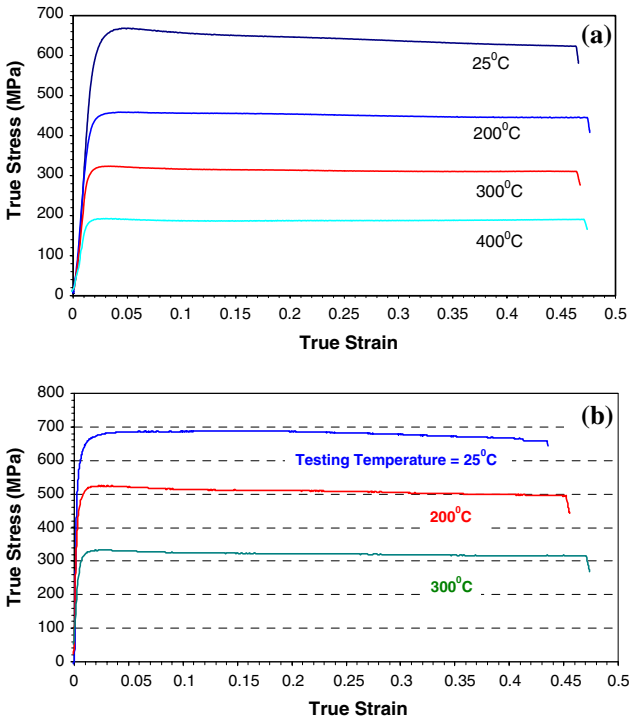

Fig. 3 Compressive true stress-true strain curves of the extruded nc $Al_{93}Fe_3Cr_2Ti_2$ alloy under a constant strain rate of 10^{-3} s^{-1} at different temperatures as indicated: (**a**) the alloy extruded at 500 °C with an average grain size of 80 nm, and (**b**) the alloy extruded at 450 °C with an average grain size of 50 nm

Figure 4 shows the typical tensile true stress-true strain curves of the extruded nc $Al_{93}Fe_3Ti_2Cr_2$ alloy deformed at different temperatures with a constant strain rate of 10^{-3} s^{-1} [29]. It is quite clear that the strain-to-failure in tension is much lower than that in compression. Furthermore, comparisons between the tensile fracture strength and the compressive strength values reveal several interesting phenomena [29]. First, the fracture strength in tension at ambient temperature is equal to the proportionality limit in compression. Second, the fracture strength in tension at 200 °C is higher than the proportionality limit, but lower than the 0.2% offset yield strength in compression. Third, the fracture strength in tension at 300 °C is higher than both the proportionality limit and the 0.2% offset yield strength, but lower than the maximum strength in compression. Finally, the fracture strength in tension at 400 °C is equal to the maximum strength in compression. Based on the TEM analysis, the aforementioned phenomena have been related to the interplay of the limited capacity of nanoscale grains in storing dislocations and the dynamic recovery of dislocation

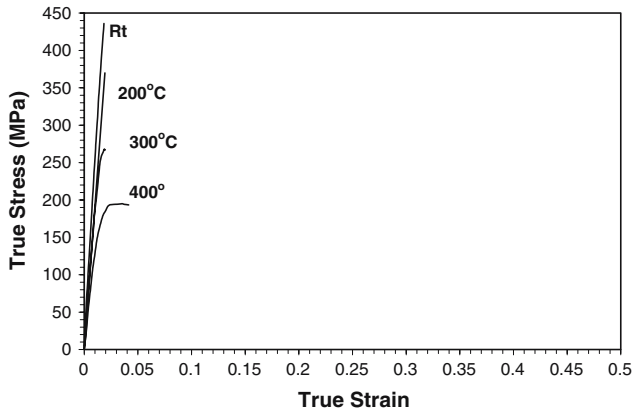

Fig. 4 Tensile true stress-true strain curves of the extruded nc $Al_{93}Fe_3Cr_2Ti_2$ alloy obtained at different temperatures with a constant strain rate of 10^{-3} s^{-1}

annihilation [29]. More detailed explanation of these phenomena will be presented in Sect. ''Comparisons between the deformation model and the experimental data.''

The Young's modulus of the extruded nc $Al_{93}Fe_3Cr_2Ti_2$ alloy as a function of temperature is shown in Fig. 5 [30]. For comparison, the elastic modulus of the 7,075 Al alloy is also measured. It is clear that the extruded nc $Al_{93}Fe_3Cr_2Ti_2$ alloy has much higher Young's moduli than the 7,075 alloy at both room and elevated temperatures. Furthermore, the elastic modulus of the 7,075 alloy is very close to that of pure Al [39]. The high modulus exhibited by the extruded $Al_{93}Fe_3Cr_2Ti_2$ alloy is believed to be due to the presence of 30 vol.% intermetallics. If the elastic modulus of the nc fcc-Al matrix is assumed to be equal to that of the pure Al, the average elastic modulus of the intermetallics, Al_3Ti and $Al_{13}Fe_4$, can then be estimated with the aid of the rule of mixtures:

$$E_c = 0.7 * E_{Al} + 0.3 * E_{int} \quad (1)$$

where E_c is the measured elastic modulus of the extruded $Al_{93}Fe_3Cr_2Ti_2$ alloy, E_{Al} the elastic modulus of the nc fcc-Al matrix, and E_{int} the average elastic modulus of the intermetallics. Using Eq. (1), the average moduli of Al_3Ti and $Al_{13}Fe_4$ are estimated to be 175, 159, 147 and 140 GPa for 25, 200, 300 and 400 °C, respectively. The estimated average modulus of Al_3Ti and $Al_{13}Fe_4$ at room temperature is close to the elastic modulus of Al_3Ti predicted from the first-principle calculation [40]. This lends the credential to the argument that the high elastic modulus of the nc $Al_{93}Fe_3Cr_2Ti_2$ alloy is due to the presence of the intermetallic precipitates. Nanocrystalline Al alloys with high elastic moduli and strengths can offer higher performance than traditional Al alloys in many stiffness-, strength- and weight-critical applications [41].

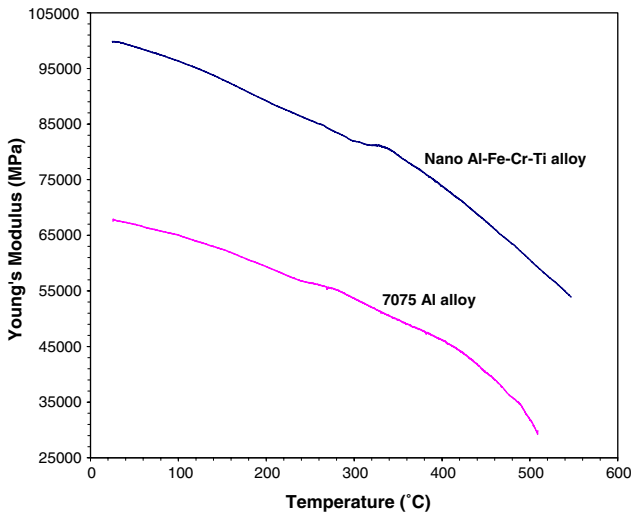

Fig. 5 Young's moduli of the extruded nc $Al_{93}Fe_3Cr_2Ti_2$ and the 7,075 Al alloy as a function of temperature determined using a dynamic mechanical analyzer

TEM analysis of the deformed NC multi-phase Al-alloy

To identify the deformation mechanisms responsible for the high strengths observed, compression tested samples have been examined using transmission electron microscopy. Figure 6 shows bright field TEM images of the nc $Al_{93}Fe_3Ti_2Cr_2$ alloy after compression tests at different temperatures. The presence of dislocations in all the deformed samples is obvious; furthermore, the dislocation density decreases substantially as the deformation temperature increases. Since there is no fluctuation in the stress-strain curve and no microstructural evidence of dynamic recrystallization, the decreased dislocation density in the samples deformed at high temperatures must result from dynamic recovery. This is consistent with phenomena observed in mc Al alloys, which show extensive dynamic recovery when the deformation temperature is higher than 200 °C [42]. This is also in good agreement with the decrease in the dislocation density as the strain rate decreases (Fig. 7). Clearly, dislocation-mediated deformation and dynamic recovery are operational in the nc $Al_{93}Fe_3Ti_2Cr_2$ alloy. Furthermore, dislocation activities are not uniform, but concentrate more in the fcc-Al grains next to the intermetallic particles. In fact, if TEM samples are prepared from compressed samples with 0.02 true strain, initiation of dislocations from the interface between the fcc-Al grain and intermetallic particle can be identified unambiguously (Fig. 8).

Comparisons of the TEM micrographs in Figs. 6 and 7 also reveal that there is no grain growth during mechanical testing. This is consistent with the expectation since this alloy has a very good thermal stability [21]. Furthermore, all of the samples presented in Figs. 6 and 7 were extruded at 500 °C, while the mechanical tests were conducted at 400 °C or below for less than 1.5 h.

Deformation model for the NC multi-phase Al-alloy

In order to explain the high compressive strengths observed, the flow stresses anticipated from Coble creep [43], Nabarro–Herring creep [44] and power-law

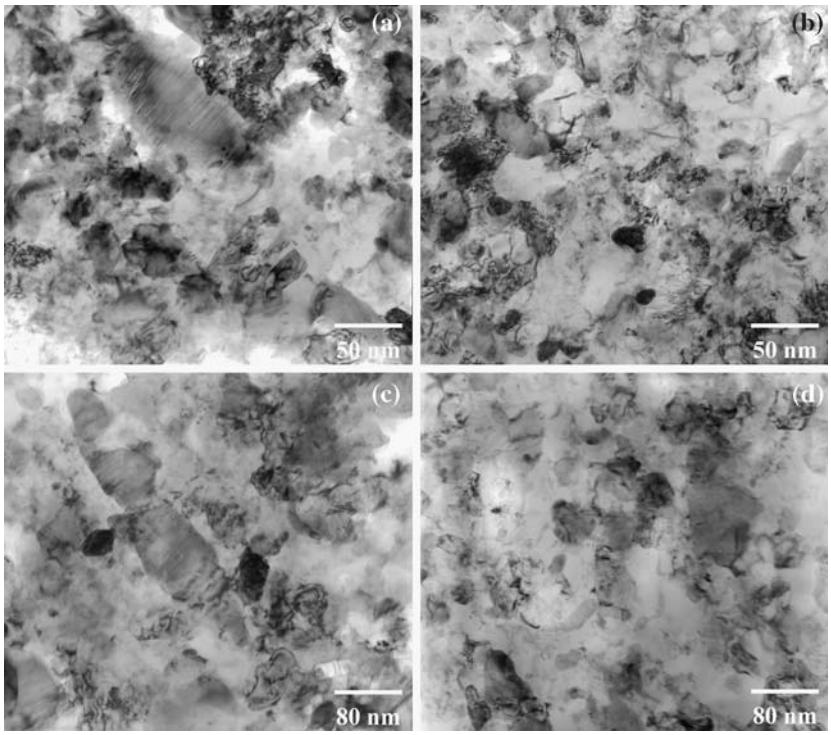

Fig. 6 Bright-field TEM images of the extruded nc $Al_{93}Fe_3Cr_2Ti_2$ alloy after compression tests with a constant strain rate of 10^{-3} s^{-1} tested at (**a**) RT (25 °C), (**b**) 200 °C, (**c**) 300 °C, and (**d**) 400 °C. Note that the dislocation density decreases with increasing the test temperature

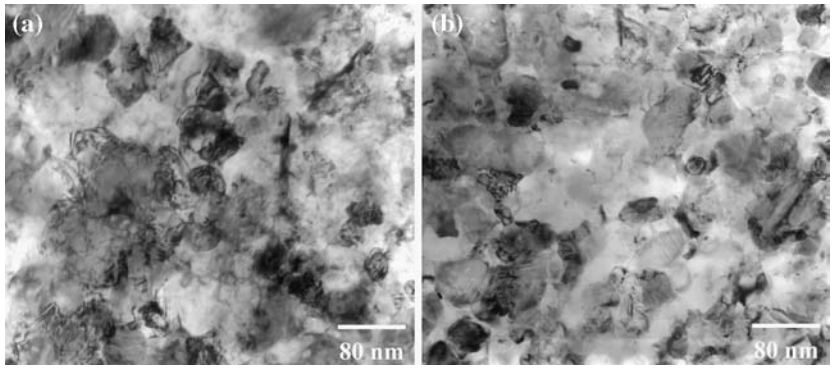

Fig. 7 Bright-field TEM images of the extruded nc $Al_{93}Fe_3Cr_2Ti_2$ alloy after compression tests at 200 °C with a constant strain rate of (**a**) 10^{-2} s^{-1} and (**b**) 10^{-4} s^{-1}. Note that the dislocation density increases with the strain rate

creep [45] for an idealized nc Al alloy composed of 30 vol.% nc intermetallic particles have been estimated. These intermetallic particles are assumed to be non-deformable, and be uniformly distributed in and separated by the nc fcc-Al matrix. Thus, at high temperatures when the nc fcc-Al matrix creeps rapidly, the intermetallic particles would ''flow'' with the matrix and the flow stress of the nc Al-alloy would be determined mainly by the creep stress of the nc Al matrix. The flow stresses for Coble creep, Nabarro–Herring creep and power-law creep of this idealized nc Al alloy are estimated using Eqs. (2), (3) and (4), respectively [43–45].

$$\sigma = \dot{\varepsilon}_{\mathrm{Al}} \frac{KT}{148\Omega} \frac{\pi d^3}{\delta D_{\mathrm{gb}}} \tag{2}$$

$$\sigma = \dot{\varepsilon}_{\mathrm{Al}} \frac{KT}{14\Omega} \frac{d^2}{D_{\mathrm{v}}} \tag{3}$$

$$\tau = \left(\frac{\dot{\gamma}_{\mathrm{Al}} kT}{AD_{\mathrm{v}}\mu_b}\right)^{1/n} \mu \tag{4}$$

where τ is the shear stress, σ the normal stress, $\varepsilon_{\mathrm{Al}}$ the normal strain rate of the fcc-Al matrix, γ_{Al} the shear strain rate of the fcc-Al matrix, d the average size of the fcc-Al grains, Ω the atomic volume of aluminum, δ the effective thickness of the grain boundary, D_{gb} the diffusion coefficient at grain boundaries, D_{v} the lattice diffusion coefficient, μ the shear modulus of the fcc-Al grains, b the Burgers vector, A the power-law creep constant, and k and T have their usual meanings.

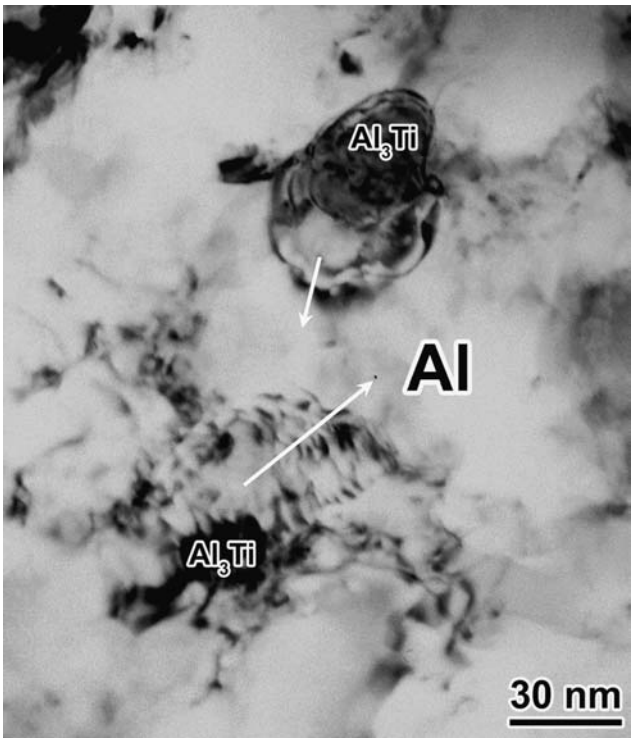

Fig. 8 Bright-field TEM image of the extruded nc $Al_{93}Fe_3Cr_2Ti_2$ alloy with 0.02 compressive strain, showing dislocations propagate into fcc-Al grains as indicated by arrows

In using Eqs. (2)–(4), the average grain size, d, is assumed to be 50 nm, and all other parameters are taken from those provided by Frost and Ashby for pure Al [39]. The application of the diffusion coefficients of pure Al in Eqs. (2)–(4) is reasonable because the nc fcc-Al grains in the extruded $Al_{93}Fe_3Ti_2Cr_2$ alloy have very low solute concentrations (Fig. 1d) and the rapid dynamic recovery at high temperatures has been unambiguously observed (Figs. 1e, 6 and 7). The effect of 30 vol.% intermetallic particles is taken into account by applying the constitutive equation derived from the potential method [46], which considers the accommodation process of the misfit strain due to the presence of non-deformable particles through heterogeneous flow of the matrix. The equation from the potential method [46] is

$$\dot{\varepsilon}_c = \dot{\varepsilon}_{Al}(1-f)^g \quad (5)$$

where $\dot{\varepsilon}_c$ is the imposed strain rate in the compression test, f the volume fraction of non-deformable particles, and g a constant being 3.2 for spherical non-deformable particles. Thus, the strain rates of the fcc-Al matrix in Eqs. (2)–(4) are given by $\dot{\varepsilon}_c = \dot{\varepsilon}_c/0.32$ and $\dot{\gamma}_{Al} = \dot{\gamma}_c/0.32$ for $f = 30\%$.

Shown in Fig. 9 is the flow stress of the diffusional creep of the nc $Al_{93}Fe_3Ti_2Cr_2$ alloy predicted using

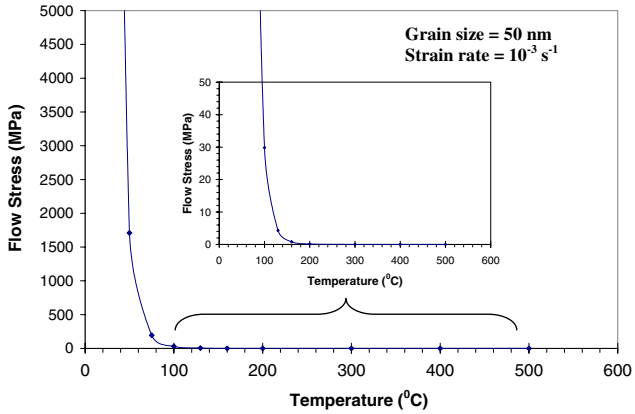

Fig. 9 The flow stress predicted using the Coble creep equation and Eq. (5). The insert magnifies the portion of the flow stresses at temperatures higher than 100 °C. Note that the theoretical strength values at elevated temperatures (>100 °C) are substantially lower than the experimental data, while near the ambient temperature the theoretical strengths (e.g., 21,770 MPa at 25°C) are much higher than the experimental values

Eqs. (2) and (5). The figure clearly reveals that the flow stress at temperatures higher than 100 °C for an imposed strain rate of 10^{-3} s^{-1} should be very low if Coble creep is operational in the nc $Al_{93}Fe_3Cr_2Ti_2$ alloy. For example, the predicted flow stress of 0.00031 MPa at 400 °C is six orders of magnitudes lower than the measured counterpart. Therefore, there is no doubt that grain boundary diffusional creep is suppressed in the nc $Al_{93}Fe_3Cr_2Ti_2$ alloy.

If Nabarro–Herring creep and power-law creep are considered, the conclusion remains the same, i.e., creep through lattice diffusion and creep via dislocation climb are also suppressed in the nc $Al_{93}Fe_3Cr_2Ti_2$ alloy. For comparison, the predicted flow stresses using Eqs. (2)–(5) corresponding to a strain rate of 10^{-3} s^{-1} are summarized in Table 1 and compared to the experimental values. Table 1 clearly indicates that at room temperature creep deformation requires very high stresses to achieve the imposed strain rate. Thus, deformation at room temperature must proceed via non-creep mechanisms for the nc $Al_{93}Fe_3Ti_2Cr_2$ alloy. Table 1 also suggests that at high temperatures if creep of the nc fcc-Al grains is not constrained, the flow stresses to achieve the imposed strain rate would be extremely low. Since the rapid dynamic recovery is observed in the nc $Al_{93}Fe_3Ti_2Cr_2$ alloy (Figs. 6 and 7), the lattice diffusion rate must be very high at elevated temperatures. However, the nc $Al_{93}Fe_3Ti_2Cr_2$ alloy exhibits a strength much higher than the flow stresses needed for unconstrained creep. Thus, it can be concluded that creep flow of the nc fcc-Al grains in the nc $Al_{93}Fe_3Ti_2Cr_2$ alloy at high temperatures has been suppressed by some non-diffusional mechanisms.

Given the observed unequivocal evidence of (i) dislocation activities, (ii) dynamic recovery, (iii) no existence of the conventional creep mechanisms at both low and high temperatures, (iv) nc fcc-Al grains with few dislocations before deformation, and (v) initiation of dislocations from the interface between the fcc-Al grain and intermetallic particle, it is proposed that the high strength exhibited by the nc $Al_{93}Fe_3Ti_2Cr_2$ alloy is dictated by propagation of dislocations into nc-Al grains. Furthermore, a semi-quantitative model based on the emission of dislocations from the interface and their propagation into fcc-Al grains is proposed herein to explain all the phenomena exhibited by the nc $Al_{93}Fe_3Ti_2Cr_2$ alloy.

Figure 10 shows the schematic of the proposed model. One of the possible mechanisms for emitting dislocations from the interface between the fcc-Al grain and intermetallic particle is presented in Fig. 10a. This mechanism is similar to the ledge model proposed by Price and Hirth [47] to describe continuous emission of screw dislocations from grain boundaries in mc metal and alloys. When a ledge at the interface is sheared one Burgers unit along the slip plane under the external stress, a screw dislocation is emitted into the fcc-Al grain. The ledge acts as a continuous source with dislocations bowing out concentrically from the active segment of the ledge. When a continuous ledge source operates in such fashion, interface sliding occurs to accommodate the shear displacement along the ledge. This interface sliding is achieved by generation of compensating interface screw dislocations similar to those described by Gleiter et al. [48]. These interface screw dislocations would bow away from the active ledge segment in the same fashion as the lattice dislocations in a manner shown in Fig. 10a. As the screw-ledge mechanism continues to operate, new ledges will be created on the faces that are not parallel to the Burgers vector of the dislocation (assuming that both faces are grain boundaries), as shown at the left and right of Fig. 10a. The height of the new ledges, h, will be given by [47]

$$h = n\,b \cdot s \tag{6}$$

where n is the number of dislocations that have passed along the ledge, b is the Burgers vector of the dislocations, and s is the unit vector normal to the tangent plane of the interface or grain boundary. The growth of the new ledges requires elastic accommodation normal to the interface and the grain boundary; this imposes a dragging force on the ends of the lattice dislocation. As result of this dragging force, the triple points at the intersections of the interface, the grain boundary and the slip plane (marked as A and B in Fig. 10a) act as pinning points and the movement of the lattice dislocation has to be achieved by further bowing. The shear stress to bow a lattice dislocation when its ends have been pinned is given by [49]

$$\tau = \frac{\mu b}{2R} \tag{7}$$

where R is the radius of curvature of the bent dislocation. As the dislocation bows away from the ledge under the shear stress, R continues to decrease until it equals half the distance between the two pinning points, l. At this point the shear stress reaches the maximum ($\tau_{max} = \mu b/l$) and the dislocation can propagate into the grain under lower shear stresses. The maximum shear stresses as a function of temperature for emitting dislocations via such a screw-ledge mechanism have been calculated using Eq. (7) with the assumption of $l = 50$ nm. The results are included in Table 1 under the heading of the predicted τ_{max} for the

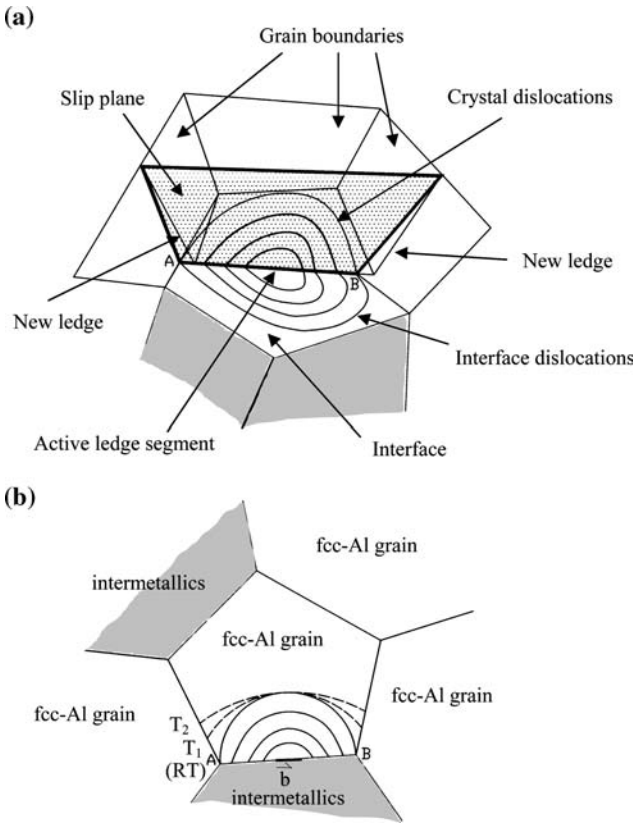

Fig. 10 (**a**) Schematic of multiple generation of screw dislocations from an active ledge segment at the interface between a fcc-Al and an intermetallic particle. (**b**) A 2D view of generation of screw dislocations from an active ledge segment at the interface, showing the dependency of the radius of curvature of the emitted dislocation on the deformation temperature ($T_2 > T_1 >$ RT)

screw-ledge mechanism. The effect of 30 vol.% intermetallic particles in the nc $Al_{93}Fe_3Ti_2Cr_2$ alloy is taken into account by assuming that the external load is carried by the nc fcc-Al grains and nc intermetallic particles. Thus, the external stress required to cause the stress-strain curve to depart from the linearity, σ_c, can be estimated via the following rule of mixtures.

$$\begin{aligned}\sigma_c &= 0.7\sigma_{max} + 0.3\sigma_{int} \\ &= 0.7m\tau_{max} + 0.3E_{int}\varepsilon_{PL}\end{aligned} \quad (8)$$

where σ_{max} is the normal stress for emitting dislocations via the screw-ledge mechanism, σ_{int} the normal stress carried by the intermetallics when the external stress reaches the proportional limit, m is the reciprocal of Schmid factor ($m = 2$ is applied here), E_{int} the average elastic modulus of the intermetallics measured from the experiment (Fig. 5), ε_{PL} the measured strain at the proportionality limit, and τ_{max} is defined in Eq. (7). The σ_c predicted using Eqs. (7) and (8) is also included in Table 1 for comparison.

Before closing this section, it should be pointed out that the continuous emission of screw dislocations from a ledge at the interface, as shown in Fig. 10a, is only one of the possible mechanisms through which dislocations can be emitted from the interface. Other mechanisms that have been proposed for emission of dislocations from the grain boundaries and interfaces of mc metals and alloys [47–51] may also be operative in the nc $Al_{93}Fe_3Ti_2Cr_2$ alloy. These other mechanisms include emission of lattice dislocations when grain-boundary dislocations move past edges or corners in the grain boundaries [48, 50], emission of lattice dislocations into two slip planes, which intersect along a grain boundary [50], and generation of edge dislocations from grain-boundary ledges [51]. However, which dislocation emission mechanism is dominating in the nc $Al_{93}Fe_3Ti_2Cr_2$ alloy is not clear at this stage. Since the strength of the nc $Al_{93}Fe_3Ti_2Cr_2$ alloy is controlled by dislocation propagation (to be discussed more in the next section), the detail of dislocation emission has limited importance. Nevertheless, identification of the dislocation emission mechanism(s) would be the interest of future studies.

Comparisons between the deformation model and the experimental data

Table 1 clearly indicates that the predicted stress needed to cause the stress-strain curve to depart from the linearity is almost identical to the measured proportionality limit for room temperature deformation. This strongly suggests that the initial yielding of the nc $Al_{93}Fe_3Ti_2Cr_2$ alloy at room temperature is controlled by propagation of dislocations into nc fcc-Al grains. However, at temperatures higher than room temperature the measured proportionality limit is lower than the predicted σ_c. This is attributed to the increased diffusion rate, which allows the aluminum atoms to diffuse to the pinning points. As such, the stress build-up at the pinning points can be partially released by the grain boundary migration and thus the position of the pinning points move towards the bowing direction of the dislocation, as shown in Fig. 10b. The exact position of the pinning points depends on the test temperature and strain rate. The higher the temperature, the farther the pinning points away from the A and B positions. Consequently, R becomes larger and the maximum shear stress to propagate dislocations into fcc-Al grains decreases. As a result, the measured proportionality limit at high temperatures is lower than the σ_c stress predicted by assuming that the pinning points are located at the A and B positions (Table 1). Similarly, increasing strain rate would result in a smaller R and thus a higher maximum shear stress to propagate dislocations. This is exactly what we have found in the experiments. As shown in Fig. 11, when the strain rate increases from 10^{-4} s^{-1} to 10^{-3} s^{-1} and 10^{-2} s^{-1}, the proportionality limit of the nc $Al_{93}Fe_3Ti_2Cr_2$ alloy at 200 °C increases from 290 MPa to 305 MPa and 315 MPa, respectively.

The model proposed above can also account for all the other phenomena observed from compression of the nc $Al_{93}Fe_3Ti_2Cr_2$ alloy. The high strain-hardening rates after yielding are due to the rapid increase in the back stresses to the propagation of dislocations into fcc-Al grains, derived from the dislocation accumulation in the nc fcc-Al grains. The strain-

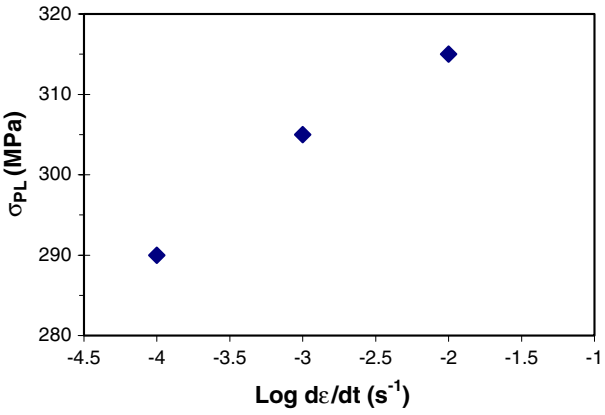

Fig. 11 The compressive proportionality limit at 200 °C for the nc Al-alloy with an average grain size of 80 nm as a function of strain rate

hardening rate decreases with increasing temperature because of the increased dynamic recovery. The small strain to the maximum strength is indicative of the limited capability of the nano-sized grains for accumulation of dislocations. The suppression of creep flow of the nc fcc-Al grains is due to the presence of 30 vol.% Al_3Ti and $Al_{13}Fe_4$ precipitates. These intermetallic particles have the same size scale as the fcc-Al grains, form a strong network in the nc $Al_{93}Fe_3Ti_2Cr_2$ alloy, and carry most of the load at high temperatures, thereby providing shield for nc fcc-Al grains.

It is noted that the model proposed is also in good accordance with the variation of the compressive strengths with grain sizes. As shown in Fig. 3, the maximum compressive strengths increase with decreasing the grain size. This phenomenon is consistent with the prediction based on the dislocation propagation process defined by Eq. (7), that is, the smaller the grain size, the higher the compressive strength.

The model can also be applied to the tensile behavior of the nc $Al_{93}Fe_3Ti_2Cr_2$ alloy if the limited dislocation storage capacity of nanoscale grains is taken into account. At ambient temperature the dislocations emitted from the interfaces accumulate in nanoscale fcc-Al grains very quickly and reach the saturation point soon after localized plastic deformation takes place (which corresponds to the proportionality limit). This induces stress concentration at grain boundaries and interfaces, and results in the formation of micro-cracks, which interlink and lead to the premature failure under tension. When the deformation temperature is increased, so is dynamic recovery. As a result, the dislocation accumulation rate within nanoscale fcc-Al grains decreases, allowing more plastic deformation before the stress concentration is high enough to induce micro-cracks. Furthermore, propagation of micro-cracks has also been impeded because of the enhanced plastic deformation capability at high temperatures to reduce the stress concentration at the crack tip. The enhanced plastic deformation capability at high temperatures is supported by the presence of more dimples at the fracture surface in comparison with that tested at ambient temperature [29]. Therefore, as temperature increases, the nc $Al_{93}Fe_3Ti_2Cr_2$ alloy starts to exhibit macroscopic yielding and eventually some ductility at 400 °C.

The analysis above clearly indicates that the lack of ductility for the nc $Al_{93}Fe_3Ti_2Cr_2$ alloy at low temperatures is due to the limited dislocation storage capacity. Several approaches to address such a challenge have been devised recently. One of the effective approaches is to introduce bimodal (or multi-modal) grain size distribution [52–54]. A microstructure with nano- and micro-grains typically exhibits adequate ductility with a limited loss of strength [52–54]. The efficacy of such a ductility-improving approach, however, remains to be investigated in nc multi-phase alloys. In addition to the bimodal grain size approach, seven other approaches for improving ductility have been reviewed recently [55]. Although not all of these ductility-improving approaches can be applied to the nc $Al_{93}Fe_3Ti_2Cr_2$ alloy, it is believed that the future research activities on this nc multi-phase alloy will heavily focus on the ductility improvement so that this nc multi-phase alloy can be embraced for engineering applications.

Finally, it should be pointed out that not all nc or ultrafine-grained multi-phase alloys exhibit the suppression of Coble or Nabarro–Herring creep at elevated temperatures. A good example of this kind is submicron-grained γ-TiAl alloys with $Ti_5(Si,Al)_3$ precipitates [56]. The high temperature deformation behavior of these γ-TiAl alloys is controlled by grain boundary sliding assisted by lattice diffusion, although the same alloys exhibit dislocation-mediated deformation (i.e., no creep deformation) at room temperature [57]. Furthermore, it is found that such lattice-diffusion-controlled deformation at elevated temperatures persists even though the volume fraction of $Ti_5(Si,Al)_3$ precipitates in the γ-TiAl alloys has been increased from 9.6 to 30 vol.% [56]. By comparing the behavior of these alloys with that of the nc $Al_{93}Fe_3Ti_2Cr_2$ alloy, it appears that in order to suppress creep flow, one of the multiple phases in the nc alloy should be resistant to deformation at elevated temperatures. The nc Al_3Ti and $Al_{13}Fe_4$ precipitates in the nc $Al_{93}Fe_3Ti_2Cr_2$ alloy clearly play such a role so that creep flow is suppressed and thus dislocation-mediated deformation becomes operative at elevated temperature.

Concluding remarks

Deformation behavior and mechanism of a nc multi-phase Al alloy have been investigated in this study. The results indicate that nc multi-phase alloys can be designed to have excellent compressive strengths at both ambient and elevated temperatures that are much higher than those possessed by the mc counterparts. If the microstructure of the nc multi-phase alloy is properly designed, deformation behavior will be controlled by propagation of dislocations into nc grains. At elevated temperatures at which dynamic recovery becomes operational, deformation behavior will be dictated by dislocation propagation and dynamic recovery. To suppress creep flow, one of the multiple phases in the nc alloy should be resistant to deformation at

elevated temperatures. Once deformation is controlled by propagation of dislocations, the smaller the grain size, the higher the compressive strengths at both ambient and elevated temperatures. The low fracture strength and lack of ductility in tensile tests remain to be serious challenges for this nc multi-phase alloy. Therefore, it is expected that the future research activities on this nc multi-phase alloy will heavily focus on the ductility improvement so that this nc multi-phase alloy can be embraced for engineering applications.

Acknowledgments The authors are grateful to Dr. Daniel Miracle at the Air Force Research Laboratory, Materials and Manufacturing Directorate, Wright-Patterson AFB, Ohio for insightful discussion on deformation mechanisms of nanocrystalline materials.

References

1. Wang YM, Chen MW, Zhou F, Ma E (2002) Nature 419(31):912
2. Legros M, Elliot BR, Rittner MN, Weertman JR, Hemker KJ (2000) Phil Mag 80 (4) 1017
3. Tellkamp VL, Melmed A, Lavernia EJ (2001) Metall Mater Trans A 32A:2335
4. Witkin D, Lee Z, Rodriguez R, Nutt S, Lavernia EJ (2003) Scr Mater 49:297
5. Wang YM, Ma E, Chen MW (2002) Appl Phys Lett 80(13):2395
6. Kumar KS, Suresh S, Chisholm MF, Horton JA, Wang P (2003) Acta Mater 51:387
7. Hugo RC, Kung H, Weertman JR, Mitra R, Knapp JA, Follstaedt DM (2003) Acta Mater 51:1937
8. Schuh CA, Nieh TG, Iwasaki H (2003) Acta Mater 51:431
9. Sanders PG, Eastman JA, Weertman JR (1997) Acta Mater 45(10):4019
10. Ke M, Hackney SA, Milligan WW, Aifantis EC (1995) Nanostruct Mater 5:689
11. Youngdahl CJ, Weertman JR, Hugo RC, Kung HH (2001) Scripta Mater 44(8–9):1475
12. Van Swygenhoven H, Spaczer M Caro A (1999) Acta Mater 47(10):3117
13. Van Swygenhoven H, Derlet PM (2001) Phys Rev B 64:224105
14. Yamakov V, Wolf D, Salazar M, Phillpot SR, Gleiter H (2001) Acta Mater 49:2713
15. Chen MW, Ma E, Hemker KJ, Sheng HW, Wang YM, Cheng XM (2003) Science 300(23):1275
16. Liao XZ, Zhou F, Lavernia EJ, He DW, Zhu YT (2003) Appl Phys Lett 83(24):5062
17. Liao XZ, Srinivasan SG, Zhao YH, Baskes MI, Zhu YT, Zhou F, Lavernia EJ, Xu HF (2004) Appl Phys Lett 84(18):3564
18. Jia D, Wang YM, Ramesh KT, Ma E, Zhu YT, Valiev RZ (2001) Appl Phys Lett 79(5):611
19. Wei Q, Jia D, Ramesh KT, Ma E (2002) Appl Phys Lett 81(8):1
20. Carsley JE, Fisher A, Milligan WW, Aifantis EC (1998) Metall Mater Trans 29A:2261
21. Shaw L, Villegas J, Luo H, Miracle D (2003) Acta Mater 51(9):2647
22. Zhou F, Lee J, Lavernia EJ (2001) Scripta Mater 44:2013
23. Fanta G, Bohn R, Dahms M, Klassen T, Bormann R (2001) Intermetallics 9:45
24. Inoue A, Kimura H (2000) Mater Sci Eng A 286(1):1
25. Kimura H, Inoue A, Sasamori K, Kita K (1998) J Jpn Inst Light Metals 48(6):263
26. Ortiz AL, Shaw L (2004) Acta Mater 52(8):2185
27. Shaw L, Luo H, Villegas J, Miracle D (2004) Scripta Mater 51:449
28. Shaw L, Luo H, Villegas J, Miracle D (2004) Scripta Mater 50(7):921
29. Luo H, Shaw L, Zhang LC, Miracle D (2005) Mater Sci Eng A 409:249
30. Luo H, Zhang LC, Shaw L (2005) J Mater Eng Perform 14(4):441
31. Shaw L, Zawrah M, Villegas J, Luo H, Miracle D (2003) Metall Mater Trans 34A(1):159
32. Massalski TB (eds) (1990) Binary alloy phase diagrams, 2nd ed. ASM International, Materials Park, OH, pp 147–149, pp 138–140, and pp 225–227
33. Erich DL (1980) AFML-TR-79-4210
34. Hayes RW, Rodriguez R, Lavernia EJ (2001) Acta Mater 49:4055
35. Yaney DL, Nix WD (1987) Metall Mater Trans 18A:893
36. Carreno F, Ruano OA (1998) Acta Mater 46:159
37. Rosler J, Joos R, Arzt E (1992) Metall Trans A 23:1521
38. Hertzberg RW (1996) Deformation and fracture mechanics of engineering materials, 4th edn. John Wiley & Sons, Inc., New York, p 18
39. Frost HJ, Ashby MF (1982) Deformation-mechanism maps. Pergamon Press, Oxford, England
40. Yoo MH, Fu CL, Lee JK (1991) Mat Res Soc Symp Proc 213:545
41. Pitcher PD, Shakesheff AJ, Lord JD (1998) Mater Sci Tech 14:1015
42. Cahn RW (1965) In: Cahn RW (ed) Physical metallurgy. North-Holland Publishing Company, Amsterdam, Netherlands, p 925
43. Coble RL (1963) J Appl Phys 34:1679
44. Herring C (1950) J Appl Phys 21:437
45. Mukherjee AK, Bird JE, Dorn JE (1969) Trans ASM 62:155
46. Lee BJ, Mear ME, Mech J (1998) Phys Solids 39:627
47. Price CW, Hirth JP (1972) Mater Sci Eng 9:15
48. Gleiter H, Hornbogen E, Baro G (1968) Acta Metall 16:1053
49. Arzt E, Ashby MF (1982) Scripta Metall 16:1285
50. Baro G, Gleiter H, Hornbogen E (1968) Mater Sci Eng 3:92
51. Li JCM (1963) Trans TMS-AIME 227:239
52. Wang YM, Chen MW, Zhou F, Ma E (2002) Nature 419(31):912
53. Wang YM, Ma E, Chen MW (2002) Appl Phys Lett 80(13):2395
54. Witkin D, Lee Z, Rodriguez R, Nutt S, Lavernia EJ (2003) Scr Mater 49:297
55. Ma E (2006) JOM 58(4):49
56. Bohn R, Klassen T, Bormann R (2001) Intermetallics 9:559
57. Bohn R, Klassen T, Bormann R (2001) Acta Mater 49:299